



Effects of two silicone resin coatings on performance of FeSiAl magnetic powder cores

Jia-qi Liu¹ · Zheng-qu Zhu¹ · Pu Wang¹ · Yi-fan Li¹ · Jing Pang² · Jia-quan Zhang¹

Received: 14 June 2023 / Revised: 2 September 2023 / Accepted: 5 September 2023 / Published online: 28 September 2023
© China Iron and Steel Research Institute Group Co., Ltd. 2023

Abstract

Two silicon resins with excellent thermal stability, JH1123 and JH7102, are used as the insulated agents and binders for the gas-atomized FeSiAl powder, and corresponding magnetic powder cores (MPCs) are fabricated. The insulation capability and application prospects of the two silicon resins are evaluated by comparing the magnetic properties of the coated powder and MPCs. The scanning electron microscopy, energy dispersive X-ray spectroscopy and Fourier transform infrared spectroscopy results show that uniform insulation layers are both formed on the powder surfaces. JH1123 has stronger binding ability, and the JH1123-coated powder exhibits severe agglomeration, with d_{50} (average particle size) approximately twice that of the JH7102-coated powder. Both as-prepared MPCs exhibit outstanding soft magnetic properties. Wherein, the permeability of FeSiAl@JH1123 is up to 74.0, which is 35.5% higher than that of FeSiAl@JH7102 because JH1123 can further improve the density of the MPCs. As for FeSiAl@JH7102, it has better direct current bias and lower core loss of 716.9 mW cm^{-3} at 20 mT and 1000 kHz due to its lower coercivity and greater anti-magnetic saturation ability. A comprehensive comparison shows that FeSiAl@JH1123 is suitable for medium and high frequency applications, while FeSiAl@JH7102 is more suitable for high frequency applications. This indicates that the use of JH1123 and JH7102 silicon resins for binding and insulated coating not only simplifies the preparation process of MPCs, but also enables the controlled production of MPCs for different applications.

Keywords FeSiAl · Insulated coating · Magnetic powder core · Permeability · Core loss

1 Introduction

Magnetic powder cores (MPCs) are a typical soft magnetic composite prepared by mixing and compressing ferromagnetic powder, insulating medium and binder based on the conventional powder metallurgy process [1, 2]. Due to ideal soft magnetic properties within a broad frequency range, MPCs are widely used as key electronic components in switching power supplies, filters, inductors, transformers, new energy vehicles and smart devices [3–6]. With the

strategy of the “energy-saving and emission reduction”, electrical and electronic devices have placed higher demands on the electromagnetic energy conversion and storage efficiency of MPCs [7, 8]. Therefore, the development of the new generation of MPCs with high permeability and low core loss under high frequency is of great significance for the realization of high efficiency and miniaturization of electromagnetic devices [9, 10].

As a representative Fe-based soft magnetic material, FeSiAl (also known as Sendust alloy) is one of the main raw materials of MPCs with the advantages of high permeability, high saturation magnetization strength, low coercivity, high resistivity and low cost [11]. However, as the operating frequency of electronic components gradually increases above the MHz range, the high-frequency applications of conventional FeSiAl MPCs are limited by the excessive eddy current loss and the resulting severe temperature rise [12, 13]. With the insulated coating as an important way to improve the high-frequency soft magnetic properties of MPCs [14], extensive research has been

✉ Pu Wang
wangpu@ustb.edu.cn

✉ Jia-quan Zhang
jqzhang@metall.ustb.edu.cn

¹ School of Metallurgical and Ecological Engineering, University of Science and Technology Beijing, Beijing 100083, China

² Qingdao Yunlu Advanced Materials Technology Co., Ltd., Qingdao 266232, Shandong, China

carried out in recent years on the design of novel insulation layers for FeSiAl MPCs. Li et al. [13] used an organosilane modified water-soluble silicone as insulated coatings and the as-prepared FeSiAl MPCs exhibited excellent insulating properties and high frequency characteristics with μ_e (permeability) of 57 at 1 MHz and P_{cv} (core loss) of 216.53 mW cm⁻³ at 100 mT and 100 kHz. The phosphate coatings prepared by conventional phosphoric acid passivation methods are brittle and porous. Based on this, Li et al. [15] prepared FeSiAl MPCs using a triple phosphate-sodium silicate-silicone resin insulation treatment and conducted a detailed study on the reaction pattern between insulation medias for different phosphoric acid concentrations. The results showed that when the phosphoric acid concentration was 3 wt.%, the MPCs possessed the optimal overall performance with a permeability of 50.91 and a core loss of $P_{cv} = 136.61$ mW cm⁻³ at 50 mT and 100 kHz [15]. Li et al. [16] designed a SiO₂-TiO₂ composite insulation layer for FeSiAl MPCs, and the MPCs after annealing at 973 K had a high permeability of 61.6 and a core loss of $P_{cv} = 118.9$ mW cm⁻³ at 50 mT and 100 kHz. In addition, the corrosion resistance and mechanical strength of the MPCs were also effectively improved by this composite coating. However, the preparation method of composite coatings has problems such as complicated steps, low production efficiency, and strict requirements for reaction temperature and reagent addition.

In recent years, advances have been made in the optimization of the insulated coating process, and the performance of commercial FeSiAl MPCs has been improved year by year. However, some of the emerging insulation layers face common problems like low production efficiency, complicated mechanisms and narrow process windows, which make it difficult to realize industrial production at present. Recently, a silicon resin with high-temperature resistance, poly-silicon-containing ary-lacetylene (PSA) resin, has been reported, which has excellent thermal stability and insulating ability due to its unique alkyne bond and chain structure, and can effectively broaden the annealing process window of MPCs [16–18]. In this study, two silicon resins with excellent thermal stability were used to prepare FeSiAl MPCs without using other binders and insulating agents, and the properties of the coated powder and MPCs were characterized to evaluate the differences of the insulation and binding capabilities of the two silicon resins in order to provide practical guidance for the industrial production of FeSiAl MPCs.

2 Numerical and experimental methods

2.1 Model assumption and governing equations

In this study, the gas-atomized FeSiAl (85.7 wt.% Fe–8.7 wt.% Si–5.6 wt.% Al) raw powder was obtained from Qingdao Yunlu Advanced Materials Technology Co., Ltd., China, and the JH1123 and JH7102 resins were purchased from Guangzhou Jiamo Chemical Technology Co., Ltd., China. All chemical reagents were of analytical purity.

Firstly, 400 g of the above FeSiAl powder was granulated and 3 wt.% silicon resins (JH1123 and JH7102) and 10 wt.% of acetone were added respectively, and then mechanically stirring was carried out for 30 min until the acetone evaporated completely. Afterwards, the above powder was screened through a 50-mesh standard sieve, dried for 1 h and then screened through a 100-mesh standard sieve to obtain the coated powder. Among them, P0, P1 and P2 are used to represent FeSiAl raw powder, JH1123-coated powder and JH7102-coated powder, respectively.

2 g of the above coated powder was mixed with 0.4 wt.% zinc stearate and compressed into a toroidal magnetic powder core (with an outer diameter of 14 mm and an inner diameter of 8 mm) by applying 900 MPa biaxial pressure at room temperature. After compressing, the MPCs were annealed at 1023 K for 1 h to relieve the internal stress. As shown in Fig. 1, S1 and S2 are used to represent the FeSiAl@JH1123 and FeSiAl@JH7102, respectively.

2.2 Characterization of FeSiAl MPCs

The morphology and element distribution of the powders were observed by scanning electron microscopy (SEM, LEO-1450, America) equipped with energy dispersive X-ray spectroscopy (EDS, NORAN-7 EDS, America). The phase identification of the powders was characterized by X-ray diffraction (XRD, D2 PHASER, Germany) using Cu K α radiation with wavelength λ of 0.154184 nm. The step size was 0.02°, the scanning range was 20°–100°, the tube voltage was 30 kV and the tube current was 10 mA. The



Fig. 1 Pictures of as-fabricated FeSiAl MPCs (S1 and S2)

characteristic functional groups of the powder were determined by Fourier transform infrared spectroscopy (FTIR, iS50, America). The size distribution of FeSiAl and coated powders was obtained using the laser-diffraction particle-size analyzer (BT-9300S, China). The detection particle size range was 0.1–1500 μm , the shading rate was set as 8.42%, the refractive index of the medium was set as 1.333, and the refractive index of the sample was set as 2.860. M_s (saturation magnetization) and H_c (coercivity) of the powder were measured using the vibrating-sample magnetometer (VSM, Lake Shore 8604, USA) under the maximum applied magnetic field intensity of ± 796 and $\pm 16 \text{ kA m}^{-1}$. The resistivity of the powder was obtained by the four-probe method using automatic powder resistivity tester (ST2742B, China). The core loss of MPCs was measured by B-H curve analyzer (SY-8219, Japan). The direct current (DC) bias performance was characterized by Lenz capacitor resistance meter (3265B, UK). μ_e was also obtained from the inductance value measured by the Lenz capacitor resistance meter (3265B, UK) at the frequency of 0–1000 kHz, and the calculation method can be found in our previous study [19]. The density and porosity of SMCs were measured using the electronic density tester (HZK-JA510) and vacuum moisture-proof box (VE-ALL). Herein, according to the standard GB/T 5163–2006, the density ρ and porosity P of SMCs can be calculated by Eqs. (1) and (2), respectively.

$$\rho = \frac{m_0}{m_a - m_w} \rho_w \quad (1)$$

$$P = \frac{m_a - m_0}{m_a - m_w} \cdot \frac{\rho_w}{\rho_o} \quad (2)$$

where m_0 represents the mass of samples in the air; m_a represents the mass of oil-immersed samples in the air; ρ_w represents the density of water at the test temperature T ; m_w represents the mass of oil-immersed samples in the air; and ρ_o represents the density of oil at the test temperature T .

3 Results and discussion

3.1 Powder performance characterization

Figure 2a, c, e shows the SEM pictures of P0, P1 and P2, and Fig. 2b, d, f presents the particle size distribution curves of the corresponding powder, respectively. As seen in Fig. 2a, most of the FeSiAl particles are nearly spherical with an average sphericity of 0.89 (details can be seen in Fig. S1), and the surfaces are relatively smooth without satellite powder, needle-shape powder and other defects,

which is conducive to the formation of uniform insulated coatings [20]. d_{50} (average particle size) and the standard particle size deviation d_{84} (particle size at the cumulative percentage of 84%)/ d_{50} are 32 μm and 1.93, respectively, which indicates that FeSiAl raw powder has a fine but disperse size distribution. Therefore, the subsequent processing of the raw powder needs to be properly granulated to improve the powder fluidity and moldability. The powder surfaces are still relatively smooth after insulated coating, but there are different degrees of agglomeration for both P1 and P2 under the binding effect. Since the binding ability of JH1123 is significantly stronger than that of JH7102, the agglomeration degree of P1 is significantly stronger than that of P2, which in turn leads to d_{50} of P1 powder (68 μm) being much larger than that of P2 powder (38 μm). Moreover, after treated by JH1123, most of the small particles can adhere to other particles, resulting in the narrower size distribution and much smaller d_{84}/d_{50} of P1 (1.68) than that of P2 (1.87).

To further confirm the coatings on the surfaces of FeSiAl powder, EDS and FTIR examinations were performed. The XRD diffraction patterns of P0, P1 and P2 are shown in Fig. 3. Among them, three diffraction peaks are all observed in the XRD patterns of P0, P1 and P2, corresponding to the (220), (400) and (422) crystal planes of face-centered cubic (fcc) $\text{Al}_{0.3}\text{Fe}_3\text{Si}_{0.7}$ (JCPDS No. 45-1206) [21]. The intensities of the three diffraction peaks for P1 and P2 are weaker than that for P0 because the volume fraction of $\text{Al}_{0.3}\text{Fe}_3\text{Si}_{0.7}$ is reduced due to the addition of non-ferromagnetic resins. In addition, no diffraction peaks corresponding to other phases are detected for both P1 and P2. Combined with the previous studies, the reasons for this phenomenon may be: (i) JH1123 and JH7102, as organic polymers, are amorphous with diffuse scattering peaks; (ii) the content of resins added in this study is too low to be detected by XRD [17, 19, 22].

Figure 4a–d shows the EDS analysis results for P0, P1 and P2. For P0, as shown in Fig. 4a, d, the spherical particles have a uniform elemental distribution, and the elemental mass fractions are also very close to the nominal composition. After insulated coating, additional signals of C and O elements are detected in P1 and P2 (Fig. 4d), and the mass fraction of Si elements increased from $9.0 \pm 0.2 \text{ wt.}\%$ in P0 to $9.9 \pm 0.2 \text{ wt.}\%$ and $10.6 \pm 0.3 \text{ wt.}\%$, respectively. Combined with elemental distribution maps in Fig. 4b, c, the O and Si elements are also uniformly distributed on the powder surfaces, which indicates that uniform silicon resin coatings can be prepared under the insulated coating conditions in this study. The quantitative

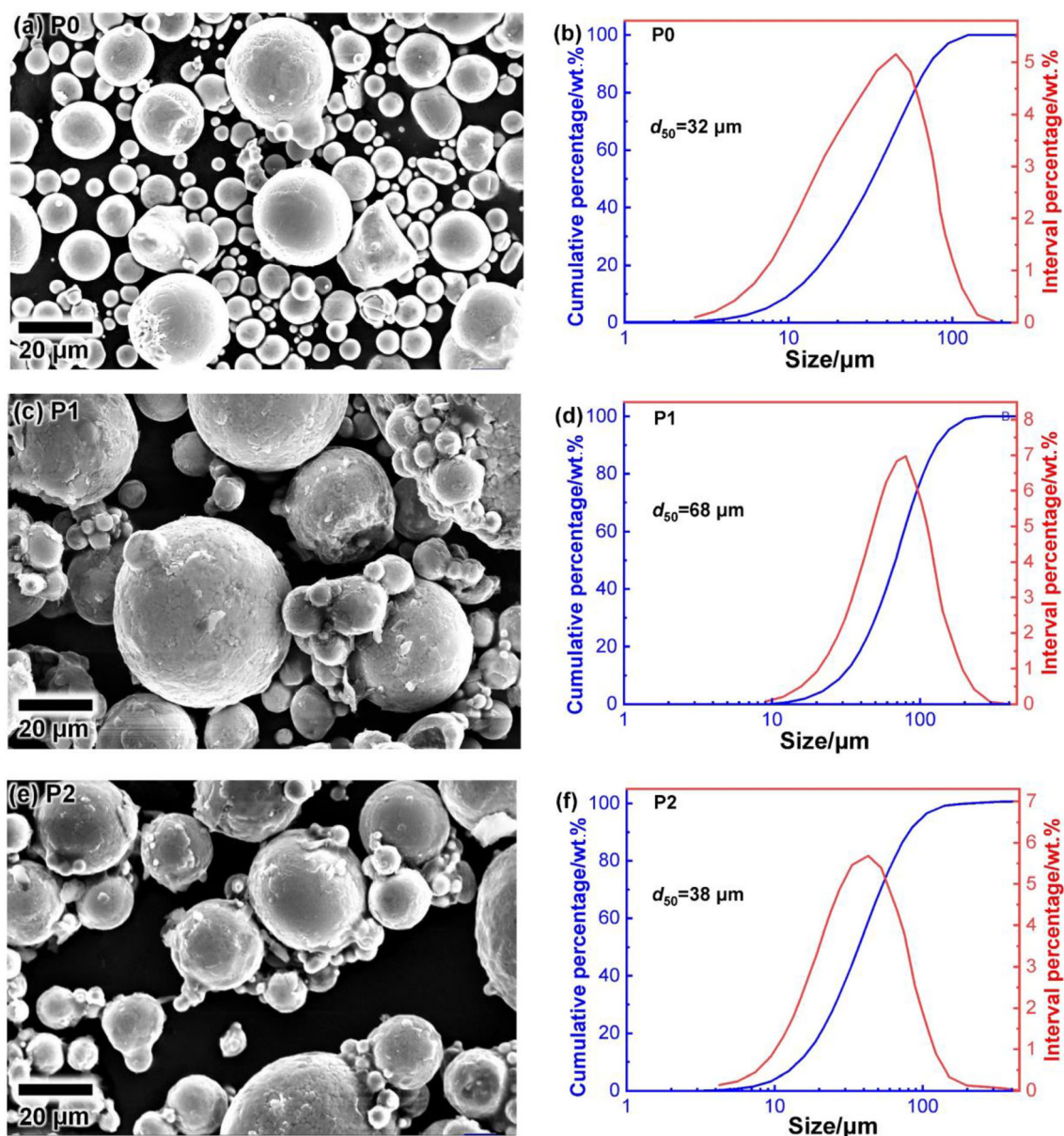


Fig. 2 SEM images and size distribution of P0 (a, b), P1 (c, d) and P2 (e, f)

results of the insulation layer composition by X-ray photoelectron spectroscopy (XPS) can be seen in Table S1.

To further characterize the two resin coatings (JH1123 and JH7102), FTIR tests were conducted as shown in Fig. 5. Compared with the raw powder P0, some characteristic peaks corresponding to organic polymers appeared in the energy spectra of P1 and P2. The absorption peak at 3299 cm^{-1} originates from the stretching vibration of alkyne hydrogen ($\equiv\text{C-H}$) [18]. The strong absorption peaks at 2916 and 2848 cm^{-1} are attributed to the stretching vibration of methylene ($-\text{CH}_2$) [18]. The absorption peak at 1635 cm^{-1} can be attributed to the stretching vibration of the $-\text{OH}$ bond in the chemisorbed

water [23]. The absorption peak at 1554 cm^{-1} may originate from the stretching vibration of the C skeleton in the phenyl ring [18]. The absorption peak at 1269 cm^{-1} corresponds to the flexural vibration of methyl ($-\text{CH}_3$) plane [18]. The absorption peaks at 1112 , 1012 and 765 cm^{-1} correspond to the ether bond (C-O-C) [18], C-O-H bond [24] and the aromatic C-H bond [25]. The above results also further demonstrate the existence of resin coatings. Furthermore, although P1 and P2 exhibit the same characteristic peaks in the FTIR spectra, obvious differences in the intensity of the characteristic peaks corresponding to each organic functional group ($\equiv\text{C-H}$, $-\text{OH}$ and $-\text{CH}_3$, etc.) can be observed. This indicates that there are

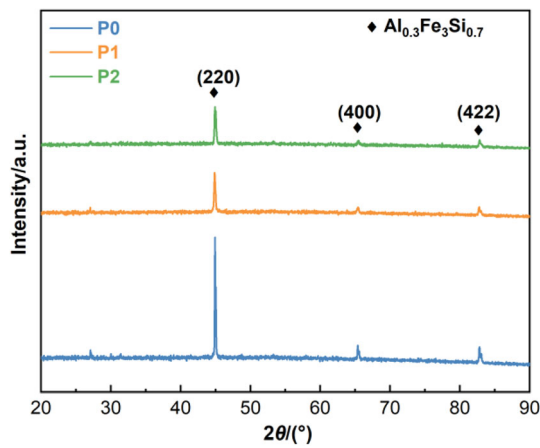


Fig. 3 XRD patterns of P0, P1 and P2. 2θ —Diffraction angle

differences in the structures of JH1123 and JH7102, and this is the fundamental reason for their different performance.

The measured hysteresis loops are shown in Fig. 6, and the related data are listed in Table 1. The hysteresis loops of P0, P1 and P2 all exhibit the typical characteristics of soft magnetic materials, and M_s of P0, P1 and P2 is 0.97, 0.95 and 0.93 T, respectively. M_s is related to the total volume-normalized magnetic moment [26]. Due to the addition of silicon resins, the magnetic dilution effect of the non-ferromagnetic material leads to the lower M_s of P1 and P2 powders than that of P0. Besides, M_s of P1 is larger than that of P2, and this difference can be explained by the core-shell theory (FeSiAl particles are cores and coatings are shells in this study) [27, 28].

$$M_s = M_{sc} - \frac{6\delta(M_{sc} - M_{ss})}{d} \approx \left(1 - \frac{6\delta}{d}\right)M_{sc} \quad (3)$$

where M_{sc} represents the saturation magnetization of the core; M_{ss} represents the saturation magnetization of the

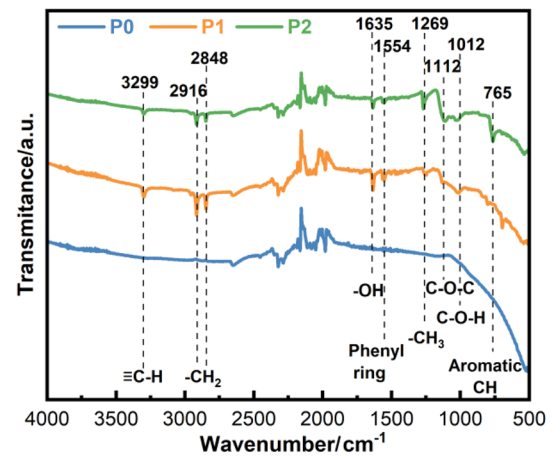


Fig. 5 FTIR analysis of P0, P1 and P2

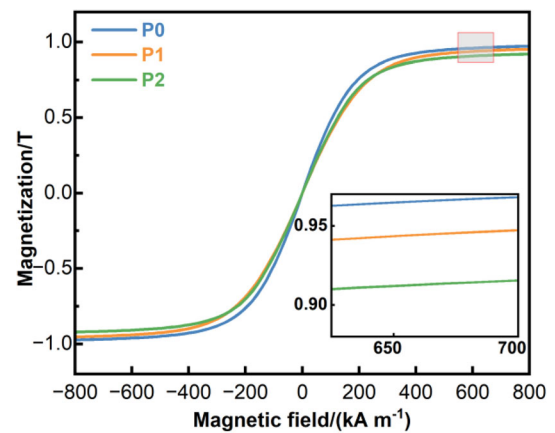


Fig. 6 Hysteresis loops of P0, P1 and P2

shell; δ represents the thickness of the shell; and d represents the diameter of powders. Since M_s of non-ferromagnetic silicon resins is approximately 0, M_s of powder with core-shell structure can be determined by Eq. (3).

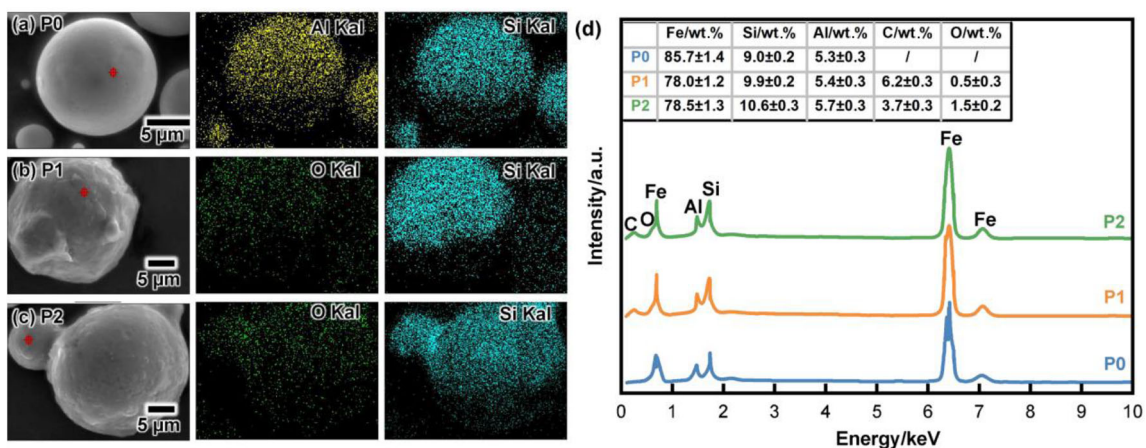


Fig. 4 Element distribution maps of P0 (a), P1 (b) and P2 (c) and EDS spectra of P0, P1 and P2 (d)

Table 1 Measured powder properties of P0, P1 and P2

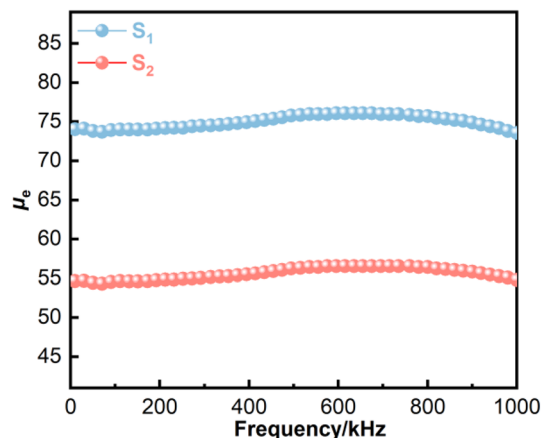
Sample	$d_{50}/\mu\text{m}$	d_{84}/d_{50}	M_s/T	$H_c/(A\text{ m}^{-1})$	Resistivity/ $(\Omega\text{ cm})$
P0	32	1.93	0.97	28.6	745
P1	68	1.68	0.95	48.5	78,180
P2	38	1.87	0.93	34.2	2630

Under the same concentration conditions, the thickness of the shell layer can be considered approximately the same, while d_{50} of P1 is much larger than that of P2, so that M_s of P1 is higher than that of P2. H_c of the powder is shown in Table 1, and P1 and P0 have the highest and lowest coercivity, respectively. Coercivity is a structurally sensitive physical quantity, which is mainly related to factors such as purity, internal stress and defects [29]. H_c is higher in the coated powder due to the introduction of insulated coatings. Whereas, H_c of P1 is higher than that of P2 due to the stronger binding ability of JH1123 and the stronger resistance to the rotation and displacement of the magnetic domain walls in P1 [30].

3.2 Comparison of soft magnetic properties of MPCs

The measured density and porosity of the MPCs based on Eqs. (1) and (2) are shown in Table 2 below. P1 has better moldability, S1 has a higher density than S2, and the internal porosity of S1 is only 14.05%.

Permeability is a physical quantity that evaluates the ability of magnetic functional materials to magnetize under an applied magnetic field and is one of the important performance parameters of MPCs, which is mainly related to the density, porosity, non-ferromagnetic material content, particle size and internal defects of MPCs [16, 31]. The variation of μ_e of S1 and S2 with frequency is shown in Fig. 7. In the frequency range from 0 to 1000 kHz, and the decrease in μ_e of S1 and S2 is slight with increasing frequency, both of which exhibit excellent frequency stability. In general, μ_e increases with the increase in density and ferromagnetic material content of MPCs. Moreover, based on the results of previous related experiments, μ_e increases with increasing particle size, although the frequency stability deteriorates [19, 32]. In this study, S1 has higher

**Fig. 7** Trend of effective permeability of S1 and S2 with frequency

density and thinner insulation layer (relevant calculations can be seen in Tables S2 and S3), and d_{50} of P1 is also much larger than that of P2, so that $\mu_e@100\text{ kHz}$ of S1 (74.0) is much larger than that of S2 (54.6).

When electronic components serve in a circuit, the permeability inevitably decreases with the increase in the superimposed DC magnetic field strength, leading to the deterioration of the operational performance of the electronic devices. Under the current trend of high current and high power in electronic components, improving the DC bias performance of MPCs by delaying the magnetic saturation process of soft magnetic materials is an effective way to improve the soft magnetic performance of electronic components under high DC bias magnetic fields [17]. The DC bias performance can be characterized by the percentage permeability $\mu_{e\%}$ (the ratio of the permeability under the DC bias field to the permeability without the DC bias field), and a comparison of the DC bias performance of S1 and S2 can be seen in Fig. 8. $\mu_{e\%}$ of S1 and S2 decays with the DC magnetic field gradually increasing up to 7958

Table 2 Density and porosity of S1 and S2

Sample	m_o/g	m_w/g	m_a/g	T/K	$\rho_w/(g\text{ cm}^{-3})$	$\rho_o/(g\text{ cm}^{-3})$	$\rho/(g\text{ cm}^{-3})$	$P/\%$
S1	1.979	1.675	2.022	292	0.998	0.880	5.692	14.05
S2	1.958	1.659	2.014	292	0.998	0.880	5.504	17.89

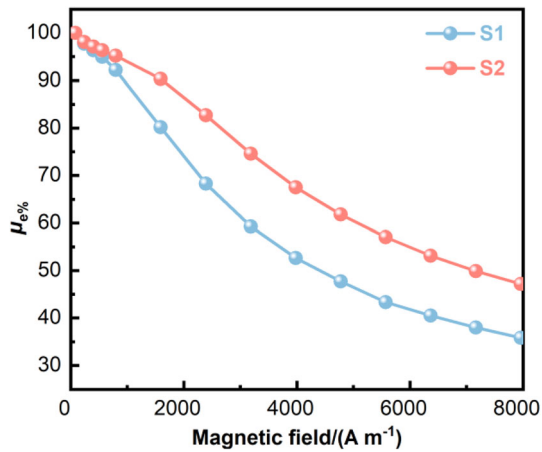


Fig. 8 Comparison of DC bias performance for S1 and S2

A m^{-1} . The DC bias performance is related to the anti-magnetization process, i.e., it is inversely associated with μ_e [10, 33]. On the one hand, S1 has higher μ_e and is more likely to reach magnetic saturation under the applied magnetic field; on the other hand, the nonferromagnetic air gaps can delay the magnetic saturation process by increasing the demagnetization field [19, 29, 34], while the porosity of S1 is lower than that of S2, so that the DC bias performance of S1 is worse than that of S2.

P_{cv} is another important performance index of MPCs, which directly determines the heat release, energy conversion efficiency and service life of electronic components under an alternating electromagnetic field [33, 35]. Based on the classical loss separation theory, P_{cv} can be divided into hysteresis loss P_h , eddy current loss P_e and excess loss P_{ex} [36, 37]. Herein, P_{ex} has high values only at very low induction level and very high frequency and can be neglected in high power electronic component applications [38]. Therefore, P_{cv} can be expressed by Eq. (4):

$$P_{cv} = P_h + P_e + P_{ex} \approx K_h B_m^3 f + \frac{CB_m^2 f^2 d_0^2}{\rho_e} \quad (4)$$

where K_h is the hysteresis loss coefficient; B_m is the magnetic induction intensity; f is the frequency; C is a constant; d_0 is approximately equal to the particle size; and ρ_e is the resistivity of MPCs. Under $B_m = 20$ mT, the measured P_{cv} of S1 and S2 in the range of $f = 100$ – 1000 kHz is presented in Fig. 9a. P_{cv} increases rapidly with frequency, and P_{cv} of S1 is higher than that of S2. To further analyze the loss sources of S1 and S2, loss separation is performed based on Eq. (4), and the trends of P_h and P_e with frequency are plotted in Fig. 9b, c, respectively. In general, K_h is proportional to H_c [19, 34]. As can be seen from Table 1, H_c of P1 is larger after JH1123 treatment, resulting in an increase in P_h of S1. P_e

decreases with increasing resistivity and decreasing powder size [34, 35]. Combined with the test results in Table 1, although the resistivity of P1 is higher than that of P2, the agglomeration in P1 is more serious, leading to an increase in the eddy current path and skin depth, which in turn increases P_e and is consistent with the trend of P_e for S1 and S2 in Fig. 9c.

Under the same preparation process, JH1123 has stronger binding ability, which can significantly improve the density and resistivity of MPCs, but serious particle agglomeration also arises. Although JH7102 has weaker binding ability, particles can be effectively electrically separated and thus the eddy current path can be reduced. Based on the above characterization of MPCs, S1 with high permeability ($\mu_e = 74.0$ at 100 kHz), poor DC bias performance ($\mu_{e\%} = 35.1$ at 7958 A m^{-1}) and high P_{cv} under high frequency ($P_{cv} = 984.9 \text{ mW cm}^{-3}$ at 20 mT and 1000 kHz) is more suitable for medium and high frequency applications. Although the permeability of S2 is low ($\mu_e = 54.6$ at 100 kHz), S2 exhibits excellent DC bias ($\mu_{e\%} = 46.9$ at 7958 A m^{-1}) and low high-frequency core loss ($P_{cv} = 716.9 \text{ mW cm}^{-3}$ at 20 mT and 1000 kHz) and is more suitable for high frequency applications.

The performance of S1 and S2 prepared in this study is compared with other reported MPCs in Fig. 10, and the detailed data are listed in Table 3. The FeSiAl@JH1123/JH7102 MPCs prepared in this study exhibit outstanding high permeability and low core loss under high frequency even when compared to MPCs prepared using hybrid powder and composite coatings in the previous study. The insulated coating method used in this study is a simple process that can be industrially mass-produced, which is expected to provide a new methodology for the mass production of high-performance FeSiAl MPCs.

4 Conclusions

1. The binding ability of JH1123 is stronger than that of JH7102. The JH1123-coated powder P1 suffers from severe particle agglomeration with a large d_{50} of $68 \mu\text{m}$, which is nearly twice that of the JH7102-coated powder P2. Besides, P1 has higher M_s (0.95 T), but its H_c also increases to 48.5 A m^{-1} due to the strong resistance to the motion of the magnetic domain walls.
2. Compared to JH7102, JH1123 can further improve the powder moldability. S1 has higher density and lower porosity, and although its DC bias performance is poor, the reduced content of non-ferromagnetic material results in a superior permeability ($\mu_e = 74.0$ at 100 kHz). S2 has a lower permeability than S1

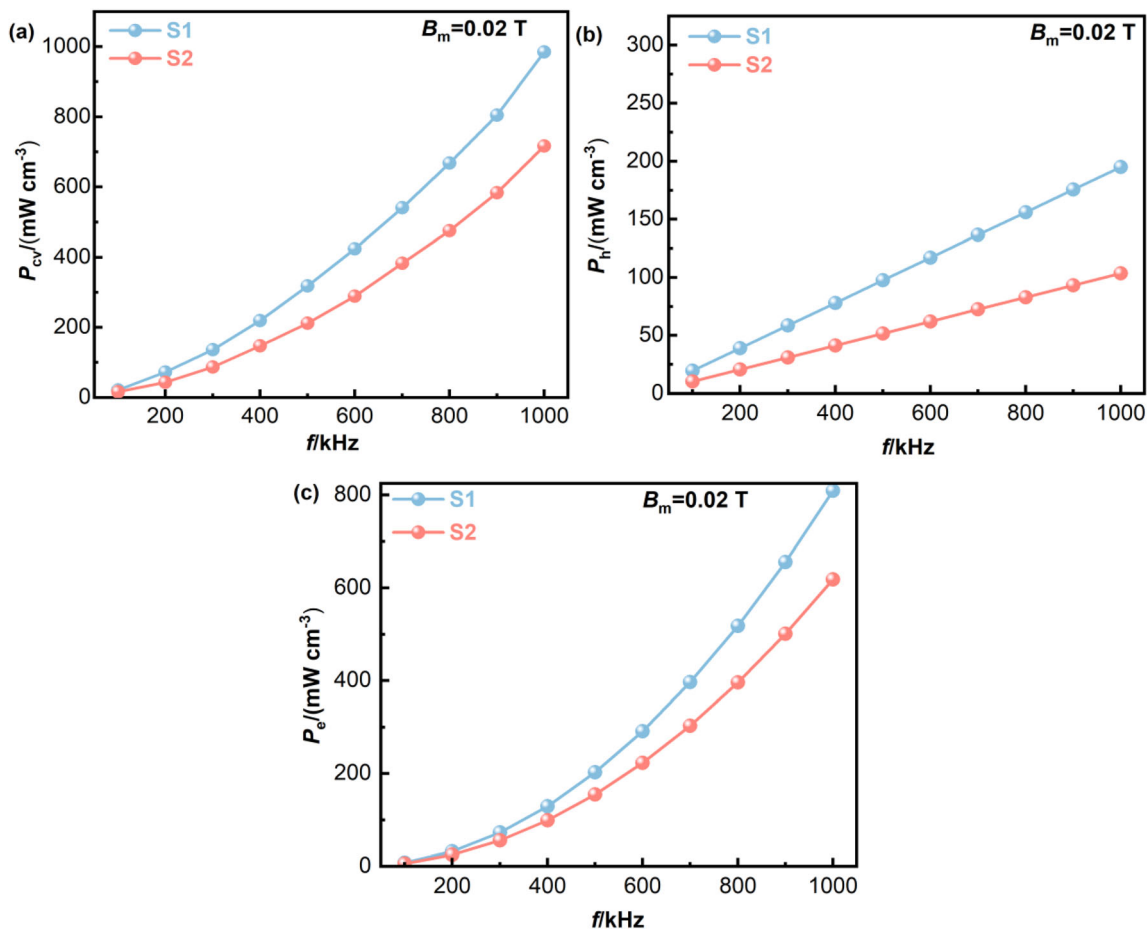


Fig. 9 P_{cv} (a), P_h (b) and P_e (c) of S1 and S2

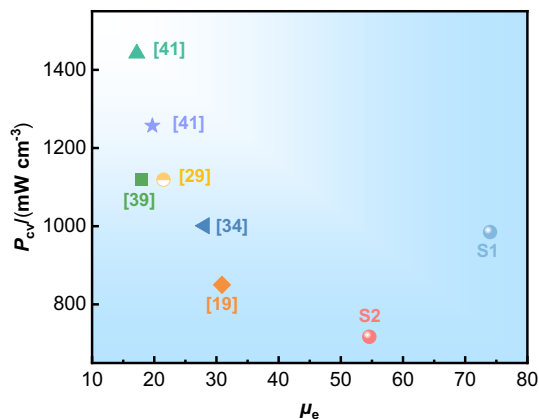


Fig. 10 Comparison of μ_e and P_{cv} between FeSiAl MPCs and reported MPCs in previous research

($\mu_e = 54.6$ at 100 kHz) due to its lower density and higher porosity, but the improved anti-magnetic saturation ability leads to better DC bias performance.

- The loss separation results show that despite the higher resistivity of P1, the higher H_c and d_{50} lead to higher hysteresis and eddy current losses of S1, and therefore, the total loss of S1 ($P_{cv} = 984.9 \text{ mW cm}^{-3}$ at 20 mT and 1000 kHz) is larger than that of S2 ($P_{cv} = 716.9 \text{ mW cm}^{-3}$ at 20 mT and 1000 kHz).
- Compared with the reported MPCs, the FeSiAl@JH1123/JH7102 MPCs prepared in this study not only have a simple preparation process, but also exhibit excellent comprehensive soft magnetic properties. Moreover, it is found that S1 has higher permeability but worse DC bias performance and higher core loss, which is more suitable for medium and high frequency range; S2 has better DC bias and lower core loss under high frequency but lower permeability, which is more suitable for high frequency applications. Therefore, by using two types of silicon resins, it is possible to achieve controlled adjustment of the soft magnetic properties of MPCs for

Table 3 Details of μ_e and P_{cv} between FeSiAl MPCs and other reported MPCs

Component	μ_e at 100 kHz	$P_{cv}/(\text{mW cm}^{-3})$		Source
		100 kHz/0.02 T	1000 kHz/0.02 T	
FeSiAl@JH1123	74.0	21.2	984.9	This work
FeSiAl@JH7102	54.6	15.9	716.9	This work
FeSiAl@Phosphate/Sodium silicate/Silicone resin	50.7	–	–	Ref. [15]
FeSiAl@Phosphate/Silicone resin	61.0	–	–	Ref. [17]
FeSiBCCr/Carbonyl iron powder@Phosphate/Epoxy resin	30.9	–	850.0	Ref. [19]
FeSiBCCr@Phosphate/Epoxy resin	21.5	–	1118.7	Ref. [29]
FeBSiC@Calcium phosphate/Epoxy resin	28.1	18.0	1001.1	Ref. [34]
FeSiNbBPMoC@Resin	18.0	52.7	1120.6	Ref. [39]
Fe@Al ₂ O ₃	36.5	398.5	–	Ref. [40]
FeSiCr@Phosphate	17.2	104.2	1442.0	Ref. [41]
FeSiCr/carbonyl iron powder@Phosphate	19.7	91.3	1257.0	Ref. [41]

electronic devices serving in different frequency ranges, exhibiting excellent potential for industrial applications.

Supplementary Information The online version contains supplementary material available at <https://doi.org/10.1007/s42243-023-01105-1>.

Acknowledgements This work was financially supported by the Key R&D Program of Shandong Province, China (Grant No. 2022CXGC020308).

Declarations

Conflicts of interest The authors declare no conflict of interest.

References

- [1] B. Yang, X. Li, R. Guo, R. Yu, *Mater. Des.* 121 (2017) 272–279.
- [2] C.B. Huang, T.C. Liu, X.Y. Wang, C.W. Lu, D.R. Li, Z.C. Lu, *J. Iron Steel Res. Int.* 22 (2015) 67–71.
- [3] J.M. Silveyra, E. Ferrara, D.L. Huber, T.C. Monson, *Science* 362 (2018) 6413.
- [4] G. Zhang, G. Shi, W. Yuan, Y. Liu, *Ceram. Int.* 47 (2021) 8795–8802.
- [5] H. Shokrollahi, K. Janghorban, *J. Mater. Process. Technol.* 189 (2007) 1–12.
- [6] O. Gutfleisch, M.A. Willard, E. Brück, C.H. Chen, S.G. Sankar, J.P. Liu, *Adv. Mater.* 23 (2011) 821–842.
- [7] J.Q. Liu, Y.N. Dong, P. Wang, H. Zhao, J. Pang, X.Y. Li, J.Q. Zhang, *J. Iron Steel Res. Int.* 30 (2023) 1142–1155.
- [8] K.J. Sunday, M.L. Taheri, *Met. Powder Rep.* 72 (2017) 425–429.
- [9] W. Li, H. Cai, Y. Kang, Y. Ying, J. Yu, J. Zheng, L. Qiao, Y. Jiang, S. Che, *Acta Mater.* 167 (2019) 267–274.
- [10] Z.H. Liu, Y.Q. Dong, X.C. Liu, H. Lu, Y. Wu, H.J. Zhang, A.N. He, J.W. Li, X.M. Wang, *J. Alloy. Compd.* 885 (2021) 160924.
- [11] P. Wang, J. Liu, Y. Dong, Z. Zhu, J. Pang, J. Zhang, *J. Mater. Res. Technol.* 23 (2023) 730–743.
- [12] X. Zhong, Y. Liu, J. Li, Y. Wang, *J. Magn. Magn. Mater.* 324 (2012) 2631–2636.
- [13] W. Li, W. Li, J. Wu, X. Han, Y. Ying, J. Yu, J. Zheng, L. Qiao, J. Li, S. Che, *Mater. Sci. Eng. B* 291 (2023) 116387.
- [14] C.B. Huang, T.C. Liu, X.Y. Wang, C.W. Lu, D.R. Li, Z.C. Lu, *J. Iron Steel Res. Int.* 21 (2014) 348–351.
- [15] Z. Li, Z. Li, H. Yang, H. Li, X. Liu, *J. Electron. Mater.* 51 (2022) 2142–2155.
- [16] H. Li, H. Yang, Z. Li, Z. Li, X. Liu, *J. Electron. Mater.* 51 (2022) 3418–3429.
- [17] H. Lu, Y. Dong, X. Liu, Z. Liu, Y. Ma, Y. Wu, A. He, J. Li, X. Wang, *J. Mater. Sci.* 33 (2022) 10131–10141.
- [18] H. Lu, Y. Dong, X. Liu, Z. Liu, Y. Wu, H. Zhang, A. He, J. Li, X. Wang, *Polymers* 13 (2021) 1350.
- [19] J. Liu, Y. Dong, P. Wang, Z. Zhu, J. Pang, X. Li, J. Zhang, *J. Non-Cryst. Solids* 605 (2023) 122166.
- [20] B.V. Neamțu, M. Pszola, A. Opreș, F. Popa, T.F. Marinca, I. Chicinaș, *Ceram. Int.* 47 (2021) 1865–1874.
- [21] X. Yi, Q. Li, Y. Peng, Y. Zhao, S. Zhu, *J. Supercond. Nov. Magn.* 34 (2021) 2957–2968.
- [22] Z.Q. Zhu, J.Q. Liu, H. Zhao, J. Pang, P. Wang, J.Q. Zhang, *Materials* 16 (2023) 1270.
- [23] D. Liu, S. Gao, Y. Zhang, S. Yu, F. Wang, *Ceram. Int.* 45 (2019) 21804–21809.
- [24] P.P. Singh, G. Nath, *Waste Biomass Valorization* 13 (2022) 2905–2916.
- [25] R. Rehman, I. Manzoor, L. Mitu, *Bull. Chem. Soc. Eth.* 32 (2018) 213.
- [26] M. Tajabadi, I. Rahmani, S.M. Mirkazemi, H.G. Orimi, *Adv. Powder Technol.* 33 (2021) 103366.
- [27] Z.Y. Wu, L. Kang, X.W. Liao, H. Kong, H.C. Wang, R. Wang, *Ceram. Int.* 49 (2023) 19870–19878.
- [28] J. Wang, X.A. Fan, Z. Wu, G. Li, *J. Solid State Chem.* 231 (2015) 152–158.
- [29] J. Liu, Y. Dong, Z. Zhu, H. Zhao, J. Pang, P. Wang, J. Zhang, *Materials* 15 (2022) 6296.
- [30] R.D. Shull, *J. Iron Steel Res. Int.* 14 (2007) No. 4, 69–74.
- [31] P. Wang, Z.Q. Zhu, J.Q. Liu, C.F. Wang, J. Pang, J.Q. Zhang, *J. Alloy. Compd.* 962 (2023) 171095.
- [32] H.J. Woo, J.H. Ahn, C.P. Kim, D.H. Choi, S. Kim, B.W. Lee, *J. Non-Cryst. Solids* 577 (2022) 121309.

- [33] S. Wu, Y. Dong, X. Li, M. Gong, R. Zhao, W. Gao, H. Wu, A. He, J. Li, X. Wang, X. Liu, *Ceram. Int.* 48 (2022) 22237–22245.
- [34] P. Wang, J.Q. Liu, Y.N. Dong, H. Zhao, J. Pang, J. Zhang, *J. Non-Cryst. Solids* 602 (2023) 122082.
- [35] T. Zhao, C. Chen, X. Wu, C. Zhang, A.A. Volinsky, J. Hao, *J. Alloy. Compd.* 857 (2021) 157991.
- [36] G. Bertotti, *IEEE Trans. Magn.* 24 (1988) 621–630.
- [37] L. Ďáková, J. Fůzer, S. Dobák, P. Kollár, Y. Osadchuk, M. Strečková, M. Fáberová, R. Bureš, P. Kurek, M. Vojtko, *IEEE Trans. Magn.* 54 (2018) 1–6.
- [38] K.Y. Huang, Y.Q. Dong, M. Liu, J.H. Ren, S.H. Lu, Z.K. Zhao, C.T. Chang, X.M. Wang, *J. Iron Steel Res. Int.* 25 (2018) 624–629.
- [39] J.G. Yeo, D.H. Kim, Y.J. Choi, B.W. Lee, *J. Electron. Mater.* 48 (2019) 6018–6023.
- [40] J. Lei, J. Zheng, H. Zheng, L. Qiao, Y. Ying, W. Cai, W. Li, J. Yu, M. Lin, S. Che, *J. Magn. Magn. Mater.* 472 (2019) 7–13.
- [41] C. Xia, Y. Peng, X. Yi, Z. Yao, Y. Zhu, G. Hu, *J. Non-Cryst. Solids* 559 (2021) 120673.

Springer Nature or its licensor (e.g. a society or other partner) holds exclusive rights to this article under a publishing agreement with the author(s) or other rightsholder(s); author self-archiving of the accepted manuscript version of this article is solely governed by the terms of such publishing agreement and applicable law.